

Cluster Analysis of Vortical Flow in Simulations of Cerebral Aneurysm Hemodynamics

Steffen Oeltze-Jafra, Member, IEEE, Juan R. Cebal, Gábor Janiga, and Bernhard Preim

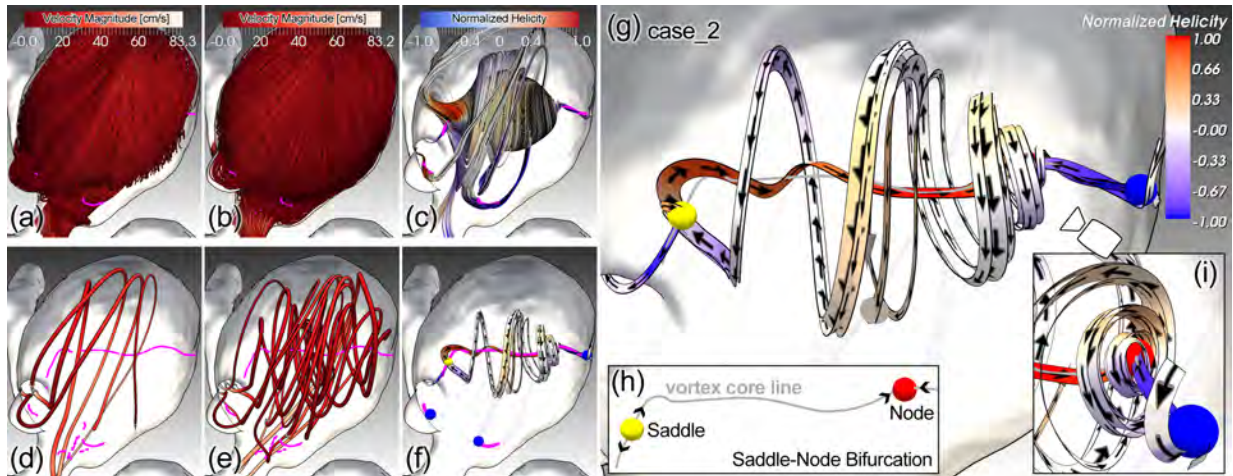


Fig. 1. Vortical flow in aneurysm with major center swirl (case #2, Fig. 9(b)). Vortex core lines are rendered magenta in (a-f). Neither streamlines seeded at the aneurysm inlet (a) or inside (b) nor the representatives (d-e) of their clustering results [32] clearly convey the swirl. We propose a new approach to grouping streamlines seeded at vortex core lines (c) comprising custom group representatives (f). It reveals an *embedded vortex* (g) — a small vortex enveloped by a larger one swirling in the opposite direction — forming around a *saddle-node bifurcation* (h). In (g-i), arrows indicate local flow direction and the vortex core line of the major swirl is rendered gray.

Abstract—Computational fluid dynamic (CFD) simulations of blood flow provide new insights into the hemodynamics of vascular pathologies such as cerebral aneurysms. Understanding the relations between hemodynamics and aneurysm initiation, progression, and risk of rupture is crucial in diagnosis and treatment. Recent studies link the existence of vortices in the blood flow pattern to aneurysm rupture and report observations of *embedded vortices* — a larger vortex encloses a smaller one flowing in the opposite direction — whose implications are unclear.

We present a clustering-based approach for the visual analysis of vortical flow in simulated cerebral aneurysm hemodynamics. We show how embedded vortices develop at *saddle-node bifurcations* on vortex core lines and convey the participating flow at full manifestation of the vortex by a fast and smart grouping of streamlines and the visualization of group representatives. The grouping result may be refined based on spectral clustering generating a more detailed visualization of the flow pattern, especially further off the core lines. We aim at supporting CFD engineers researching the biological implications of embedded vortices.

Index Terms—Blood Flow, Aneurysm, Clustering, Vortex Dynamics, Embedded Vortices

1 INTRODUCTION

Cerebral aneurysms represent a type of cerebrovascular disorder in which a weakening of the arterial wall leads to a balloon-like dilation (Fig. 2(a)). The prevalence of unruptured cerebral aneurysms in the general population has been estimated as 3.2% [48]. Their rupture is associated with a mortality rate of $\approx 50\%$.

Computational fluid dynamic (CFD) simulations of blood flow play a crucial role in understanding aneurysm rupture and evaluating its risk since they provide insights into the aneurysm hemodynamics

[4, 7, 17]. Hemodynamic parameters are evaluated as predictors for aneurysm rupture together with geometrical descriptors, wall properties, inflammatory effects, genetic predispositions, and behavioral factors. The blood flow pattern and in particular, the formation of vortices are among the hemodynamic parameters that were linked to rupture, thus motivating a detailed investigation of swirling flow [4, 7].

Previous work reports the frequent observation of *embedded vortices* — one vortex enveloped by a second one swirling in the opposite direction — in unsteady CFD simulations [3] (Fig. 1 (g)). It relates their formation and collapse over the cardiac cycle to *saddle-node bifurcations* — the collision and annihilation of a saddle and a node located on the *vortex core line* (Fig. 1 (h)). We aim at supporting CFD engineers in revealing the biological implications of embedded vortices. Here, we study the structure of these vortices at full manifestation based on a representative point of the cardiac cycle.

The investigation of embedded vortical flow benefits from an extraction of the vortex core line and the seeding of integral curves in its vicinity (Fig. 1(a-f)). In [3], groups of streamlines are integrated from manually selected core line segments which were extracted by Sujudi and Haimes' method [45]. The segments are selected and integration and visualization parameters are adjusted until inner and outer vortex are properly conveyed by a separate group of streamlines.

- S. Oeltze-Jafra and B. Preim are with the Department of Simulation and Graphics, University of Magdeburg, Germany. E-mail: {stoeltze|preim}@isg.cs.uni-magdeburg.de.
- J.R. Cebal is with the Center for Computational Fluid Dynamics, George Mason University, Fairfax, Virginia, USA. E-mail: jcebral@gmail.com.
- G. Janiga is with the Institute of Fluid Dynamics and Thermodynamics, University of Magdeburg, Germany. E-mail: janiga@ovgu.de.

Manuscript received 31 Mar. 2015; accepted 1 Aug. 2015; date of publication xx Aug. 2015; date of current version 25 Oct. 2015.

For information on obtaining reprints of this article, please send e-mail to: tvcg@computer.org.

We automate this tedious, error-prone process and contribute a fast generation of the streamline groups. The display of *group representatives* yields a comprehensive and comprehensible *visual summary* of the vortical flow (Fig. 1(g)). On demand, the groups are refined in a clustering step leading to a more detailed visualization, e.g., of flow further off the core line. We show that this two-step approach outperforms the direct clustering [32] in terms of speed and accuracy and illustrate our method by six (out of 17 investigated) case studies. We further contribute an expert evaluation of the visual summary, exploration techniques, and an automatic assembly of core line segments output by Sujudi and Haines’ algorithm [45] into continuous lines.

2 HEMODYNAMIC BACKGROUND

We introduce cerebral aneurysm hemodynamics with a focus on vortical flow and outline our hemodynamic data generation pipeline.

2.1 Hemodynamic Parameters

The role of quantitative parameters in characterizing the hemodynamic environment in ruptured and unruptured aneurysms is detailed in [6]. Here, we focus on qualitative parameters describing the blood flow pattern. They are derived from a visual inspection. If flow particles are moving mostly parallel or in a helical fashion along a common axis, the flow is considered *laminar* while *turbulent* flow is characterized by chaotic property changes. If flow from a forward stream reverses and flows back into a separation zone, *recirculation* is observed. The existence, number, and persistence of *vortices* over the cardiac cycle influence the flow *complexity* and *stability*. In complex flow, more than one recirculation zone or vortex are observed. Their disappearance and recreation during the cardiac cycle are characteristic for unstable flow.

2.2 Vortical Flow in Cerebral Aneurysms

Cebral et al. introduced and later reviewed a flow pattern classification scheme comprising flow complexity and stability [7]. Blinded observers visually classified CFD simulation results of a large database comprising ruptured and unruptured cerebral aneurysms ($n = 210$). Simple, stable patterns were seen in unruptured aneurysms while complex, unstable patterns were observed in ruptured aneurysms. More than 95% of the aneurysms contained at least one vortex. Gambaruto and João link vortex cores anchored at the aneurysm wall to *wall shear stress* and monitor the persistence of vortex cores [14]. The most rigorous investigation of vortical flow has been accomplished by Byrne et al. based on vortex core line extraction [4]. They reviewed the database from Cebral et al. [7] and expressed flow complexity by core line length, with multiple core lines, i.e., vortices, resulting in a higher overall length, i.e. complexity. The persistence of core lines was related to flow stability. Unstable, complex vortical flow was more frequently seen in ruptured than in unruptured aneurysms.

2.3 Embedded Vortices

Byrne et al. observed the formation of embedded vortices in cerebral aneurysms [3]. These vortices are characterized by a vortex layer swirling in one direction along the vortex core line, and a second vortex layer swirling in the opposite direction and enveloping the first (Fig. 2(b), top). Their formation and collapse over the cardiac cycle has been related to saddle-node bifurcations — a concept from dynamical systems theory. It describes the collision and annihilation of two *equilibrium points* with alternating stability in a dynamical system [9].¹ In one-dimensional phase space, an unstable saddle and a stable node collide at the bifurcation point and annihilate each other.

Transferred to embedded vortices, two points at which the velocity magnitude is (near-)zero, i.e. two equilibria, emerge along the vortex core line causing the formation of embedded vortical flow (Fig. 2(b)). During the cardiac cycle, they converge along the core line, collide, and disappear causing a collapse of the embedding and a regression to uni-directional vortical flow [3]. Both equilibria are of type *focus saddle* since they simultaneously exhibit stable and unstable components

¹In fluid dynamics, a saddle-node bifurcation is also referred to as *fold* or *blue skies bifurcation* and equilibria are known as *stagnation* or *critical points*.

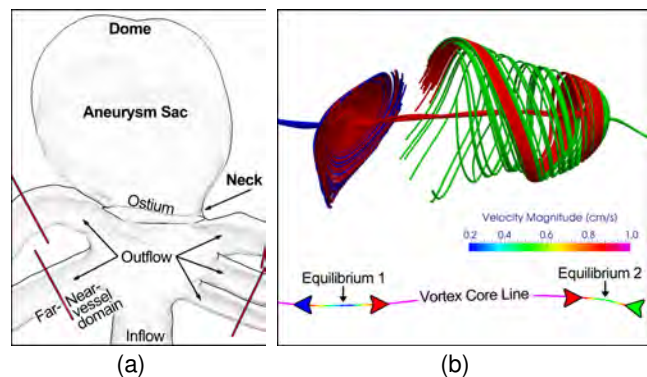


Fig. 2. (a) Morphological features (bold) of an aneurysm and subdivision of the vascular domain (red lines). (b) Embedded vortex (top) and its exposed core line (bottom). Two equilibria form a saddle-node bifurcation. Arrows indicate the saddle- (Equilibrium 1) and node-like (Equilibrium 2) flow transport along the core line. Vortex formation is detailed in the text.

— one 2D component describing the direction of swirling flow in a plane transverse to the core line (in or out relative to the equilibrium point, i.e. stable or unstable *focus*) and a 1D component describing the direction of flow transport along the core line (attracting or repelling from the point, i.e., stable node or unstable saddle). The direction of transport is expressed by stable and unstable *manifolds* also known as *stable insets* and *unstable outssets* (arrowheads in Fig. 2(b) bottom).

In Figure 2(b) top, streamlines are seeded at three manually defined core line parts separated by the equilibria. Red streamtubes spiral away from the stable focus (Equilibrium 1) along its unstable out-set (left red arrow), flow along the length of the core line and spiral in towards the unstable focus (Equilibrium 2) along its stable inset (right red arrow). As they approach the unstable focus, they collide with green streamtubes flowing in along the inset on the opposite side (green arrow). Red and green streamtubes are repelled by the unstable focus, swirl outwards, and jointly flow back along the core line.

2.4 Hemodynamic Data Generation Pipeline

The pipeline employed for the cases shown in Figure 9 (a-c) is described in the following. The pipeline for cases (d-f), which differs in steps tailored to virtual stenting, is outlined in [32].

CFD models of intracranial aneurysms are generated from 3D rotational angiography images [5]. The aneurysm and the surrounding vasculature are segmented by thresholding and region growing algorithms followed by iso-surface deformable models [49]. The resulting surface is smoothed with a non-shrinking algorithm [46]. Unstructured grids composed of tetrahedral elements are generated with an advancing front technique [25]. A maximum element size of 0.2 mm is used, resulting in meshes with approximately 1.5-3 million elements. Numerical solutions of the incompressible Navier-Stokes equations under unsteady pulsatile flows are obtained with an implicit finite element formulation and a deflated conjugate gradients solver to accelerate its convergence [28]. The *neck* of the aneurysm is manually traced on the 3D model and used to triangulate the *ostium* and subdivide the volume mesh into *aneurysm sac* and *parent vasculature* [29] (Fig. 2(a)). The latter is further subdivided into *near- and far-vessel domain* [6].

3 RELATED WORK

Post et al. categorized flow visualization techniques into direct, geometric, texture-based, and feature-based [33]. Salzbrunn et al. added partition-based techniques [38], which decompose a flow field based on vector values, integral curve properties or contained features. Our approach is related to geometric, feature-based, and partition-based techniques since we employ streamribbons to convey flow dynamics, restrict the visualization to vortices, i.e. features, and decompose the flow field around a vortex core line. We restrict our literature overview to the visualization of vortical flow and the partition-based visualization of blood flow.

3.1 Visualization of Vortical Flow

A qualitative investigation of vortical flow does not require an explicit representation of the vortex. Basic techniques such as arrow glyphs and selectively seeded streamlines were compared in this context [24]. A quantitative investigation builds upon a vortex representation, which can be the vortex core line or the vortex region. While the latter is directly visualized by a surface [43], the former serves as a basis for visualizing the flow in its vicinity, mostly by integral curves [21].

We aim at a more quantifiable and reproducible analysis of vortical flow and hence, build upon a vortex representation. We favor the core line since embedded swirling motion is better conveyed by enveloping sets of integral curves than by nested, semi-transparent surfaces. Furthermore, we need the core line to detect the equilibria constituting a saddle-node bifurcation. In the following overview of visualization approaches, we omit a description of the respective core line extraction algorithm. An introduction to extraction methods is given in [21].

Based on Vortex Core Line. The core line is often rendered as polyline or tube. Integral curves are seeded in its vicinity or cutting planes showing the local 2D flow are erected along the line [21]. Embedded vortices are visualized by means of manually defined, colored sets of streamlines in [3] (similar to Fig. 2(b) top). Filled contour plots of *normalized helicity* [27] erected along the core line facilitate the visual separation of a primary and an embedded, secondary vortex in [11]. A streamsurface tightly enclosing the core line and a color mapping to convey local flow rotation are proposed in [16]. An iconic representation of core lines is employed in [36]. A tube is colored and/or scaled according to a vortex criterion and, e.g., colored stripes on the tube indicate flow rotation. Striped pathlines around core lines for conveying vorticity transport in unsteady flow are presented in [35]. The stripes convey scalar flow quantities and simulation quality. In [37], vortex skeletons are extracted from scalar fields indicating vortex activity and visualized by tapered tubes. An illustrative rendering conveying both, vortical flow and vortex extent is introduced in [42].

3.2 Partition-Based Visualization of Blood Flow

Most techniques decompose a blood flow field into regions of similar behavior based on integral curves [2, 17, 23, 32]. Others employ local vectors [47] or aneurysm wall properties [14, 18, 30]. As argued in [50], we favor integral curves over local flow information since they represent continuous flow patterns traced over the entire domain.

3.2.1 Partitioning Based on Integral Curve Properties

Streamline predicates represent and combine local integral curve properties [39]. The predicate-based grouping of streamlines which constitute the *inflow jet* in a cerebral aneurysm is proposed in [17]. Predicates for the visual analysis of measured cardiac and aortic blood flow can be defined such that, e.g., flow passing vortices is extracted [2]. A comparison of vortex criteria for defining *pathline predicates* tailored to vortical cardiac blood flow is provided in [23].

Predicate-based approaches require the user to define attributes of interest and thresholds on attribute values. *Clustering approaches* employ a data-driven strategy for grouping integral curves and are hence self-tuning with respect to differences in the flow across datasets. In [32], different integral curve properties and techniques for clustering streamlines were compared for analyzing the blood flow pattern in cerebral aneurysms. A spectral clustering approach [51] performed best and will hence, be applied in the refinement step of our approach.

3.2.2 Partition/Cluster Representatives

A condensed visualization of clustered integral curves or fiber tracts is achieved by displaying one or more *representatives* per partition/cluster. In [50], only streamlines located at cluster boundaries are shown adhering to a user-defined density. An interactive filtering mechanism iteratively removing the most similar lines from a cluster until the characteristic ones remain is suggested in [26]. In [2], representative streamlines are derived from the skeleton of a line

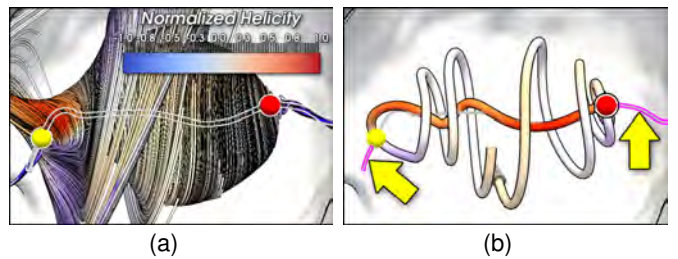


Fig. 3. (a): Streamlines seeded at core line points. The core line is superimposed and its equilibrium points are rendered as spheres (yellow: saddle, red: node). (b): Streamline clustering and display of cluster representatives [32]. The result is lacking a representation of the flow along the magenta ends (arrows) of the gray shaded core line. The same streamlines were grouped using our new approach (Fig. 1(g)). The group representatives clearly convey also the missing flow.

predicate-based streamline bundle and visualized by illustratively rendered ribbon-like structures with arrowheads. We aim at a user-independent approach exploiting the good cluster cohesion and separation achieved by our clustering technique [32]. Related work displays down to a single representative per cluster. In [8], the streamline(s) closest to the cluster centroid are computed in cluster space and displayed by streamribbons with arrowheads. Streamtubes with arrowheads are employed in [32]. Here, the streamline traversing the densest cluster parts on average is computed in streamline space employing an adaptation of [31]. We adopt the density-based representative since it does not require expensive inter-streamline similarity computations.

4 PREVIOUS APPROACHES AND NEW ANALYSIS PIPELINE

In previous work, uncluttered visualizations of the aneurysmal blood flow pattern were generated by clustering streamlines seeded at the inlet of the aneurysm, i.e. the ostium surface (Fig. 2(a)), or inside the aneurysm, and showing cluster representatives [32]. However, neither the lines (Fig. 1 (a,b)) nor their representatives (Fig. 1 (d,e)) are guaranteed to properly capture and convey (embedded) vortical flow and non-vortical flow causes visual clutter (vortices are indicated by their magenta core lines). Extracting vortex core lines and seeding streamlines in their vicinities resolves these issues (Fig. 1 (c)). However, conveying the structure of an embedded vortex requires additional efforts. In previous work, streamlines were seeded at manually selected core line parts such that inner and outer vortex were represented by a separate group of streamlines [3]. Integration length, seeding density, and transparency of the streamline groups were manually adjusted until the embedding was properly conveyed. In this tedious and error-prone process, often only trade-offs can be achieved between a clear visibility of the embedding structure, an indication of flow feeding and draining the vortex, and an uncluttered visualization also in case of multiple vortices in one aneurysm. An automated definition of the streamline groups based on the cluster representative approach in [32] and a dense set of lines seeded along the entire core line suffers from inaccuracies and performance issues. First, small parts of distinct vortical flow at core line ends are not always captured by a separate cluster (representative) hampering the assessment of local flow near equilibria (Fig. 3). This is due to the spectral clustering approach which is biased towards clusters of similar size and thus, may merge a very small cluster with a larger one [32]. Second, the clustering can take minutes depending on streamline count and length due to the employed inter-streamline similarity measure. We propose a solution that is fast, avoids visual clutter, and generates a complete visual summary of vortical flow.

Our pipeline for the cluster analysis of vortical flow is shown in Figure 4. It starts by extracting the vortex core lines from the hemodynamic data (Sec. 5.1). Since the extraction generates sets of line segments suffering from erroneous gaps and noise, continuous lines are formed in an enhancement step (Sec. 5.2). Then, streamlines are integrated from seed points along the core lines (Sec. 5.4). The subsequent clustering step comprises an initial grouping of streamlines

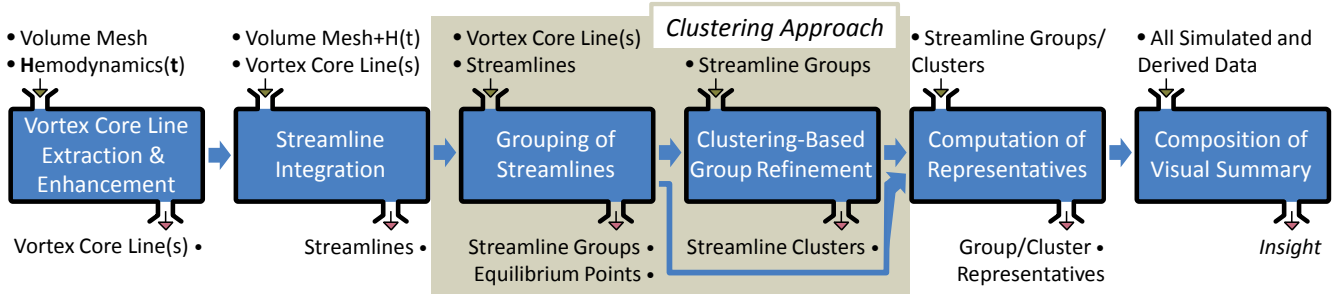


Fig. 4. Analysis pipeline. Vortex core line segments are extracted from time step t of the simulation data and continuous lines are formed in an enhancement step. Then, streamlines are integrated from core line points. Next, streamlines are grouped and the groups are optionally refined in a clustering step. Finally, group/cluster representatives are computed and integrated with other simulated or derived data in a visual summary.

and an optional refinement step. The grouping is sufficient to observe the global structure of an embedded vortex and to assess the local flow near equilibria (Fig. 1 (*f-i*)). It comprises detecting the equilibria along the core lines for defining core line partitions (Sec. 6.1) and associating each streamline with a partition (Sec. 6.2). This structured process ensures that all parts of embedded vortical flow are captured by a separate group of streamlines. It is fast since it does not require the computation of inter-streamline similarity. In an optional clustering-based group refinement, a more detailed representation of flow further off the core line and of vortical flow without an embedded structure can be achieved (Sec. 7.2). The refinement step employs the grouping result as constraint to improve accuracy and reduce computational time. After the clustering, group/cluster representatives are computed and aggregated in a visual summary of vortical flow (Sec. 8.1). The user may interact with the visual summary to explore the flow (Sec. 8.2).

5 COMPUTATION OF A VORTEX REPRESENTATION

We describe vortex core line extraction and enhancement. The core line is part of our vortex representation which is completed by streamlines integrated from seed points on the core line. Note that we consider only vortices located inside the aneurysm sac (Fig. 2(a)).

5.1 Vortex Core Line Extraction

Our collaborating CFD engineers extracted the core lines partially within previous projects employing the eigenvector method by Sujudi and Haimes [45]. It returns a line segment per element of the volume mesh that is penetrated by the core line. The set of segments is known to suffer from discontinuities between neighboring segments due to the piecewise linearity of the Jacobian and from false positives, i.e. noise. Hence, filtering mechanisms were applied.

Despite careful fine-tuning, often only trade-offs between noise removal and maintenance of “real” core line segments were achieved. Gaps resulted from a too generous filtering and the filtered data still suffers from noise (Fig. 5(a)). More sophisticated algorithms for core line extraction were proposed [40]. However, no algorithm or vortex criterion are known to guarantee vortex detection [1]. Moreover, different algorithms generate different core line candidates. To find the best algorithm is out of scope of this paper. In preliminary tests, we visually compared the given segments to the results of two algorithms implemented in EnSight (CEI Inc., Apex, NC) — the method by Sujudi and Haimes and a vorticity-based approach. The agreement also between EnSight’s methods was very high with the vorticity-based method producing more noise. A more thorough comparison involving more approaches would be required for implementing our approach in a clinical setting requiring maximum confidence. However, we focus on supporting the research endeavors of CFD engineers who are aware of the vortex extraction issues.

We stick with the available core line segments and propose an enhancement approach incorporating automatic removal of the remaining noise, gap closure, and the formation of continuous lines adhering to the segments (Sec. 5.2). In a sensitivity analysis, we visually verify all core line candidates and elaborate on the rate of false-positive and -negative (missing) core lines after enhancement (Sec. 5.3).

5.2 Vortex Core Line Enhancement

The enhancement step may neglect the flow field since we do not aim at the precise core line but at a solid base for seeding streamlines and computing equilibria. We identify curve-shaped clusters of segments, e.g., the green and red cluster in Figure 5(a), and per cluster, find the shortest path P along the segments from one end of the curve/cluster to the other (Fig. 5(c)). Gaps are closed by merging nearby, similarly oriented paths P . Stair-case artifacts caused by discontinuities between adjacent segments are resolved by smoothing (Fig. 5(b)). The proposed approach can handle multiple core lines but fails to handle branching ones. So far, we did not observe branching vortex cores.

Clustering. At first, the segments are clustered using a density-based technique (Fig. 5(a)). Such techniques are particularly suited for noisy data and non-spherical clusters. Instead of employing the line segments, we cluster their endpoints. This is feasible since the endpoints of a segment are very close together due to their location inside the same cell of the volume mesh. We employ a variant of the DBSCAN clustering algorithm that requires only a single parameter $minPts$ steering the minimum number of points to be considered as a cluster [10]. The second parameter ϵ of the original DBSCAN algorithm is derived from $minPts$. It represents the distance between points up to which they are considered to lie in the same cluster. Small clusters can be tagged as outliers, i.e. false positives, by adjusting $minPts$. However, increasing $minPts$ leads to larger values of ϵ which in turn leads to the merging of outliers with larger clusters in close proximity. We thus set $minPts = 1$ and skip small clusters when determining P .

Graph Representation. In a second step, the set of points is treated as undirected, edge-weighted graph. Each of the n points corresponds to a node. An edge exists between two nodes if their points are contained in the same cluster. The Euclidean distance is employed as edge weight unless the points belong to the same line segment, in which case a predefined value very close to zero is assigned. This guarantees that the search for the shortest path P prefers the line segments. For instance, P of a U-shaped set of segments would otherwise correspond to the direct connection of the U’s ends. The graph is represented by its sparse $n \times n$ adjacency matrix A .

Shortest Path Search. A series of steps is carried out to determine P_c for each cluster c . Clusters smaller than a threshold T_1 are neglected since they are likely to represent false positives (too small clusters in Fig. 5(a)). (1) For the rest, the corresponding subgraph A_c is extracted from A . A straightforward but expensive approach to search for P_c would be the computation of all shortest paths between pairs of nodes in A_c with P_c being the longest of them. (2) To minimize the number of pairs to test, the *minimal spanning tree* MST_c of A_c is computed [34] (black structure in Fig. 5 (close-up)). It forms a natural skeleton of c suggesting its shape. (3) Then, the shortest paths between all pairs of nodes in MST_c are computed [22] and the longest of them P_{tmp_c} is memorized (yellow path in Fig. 5 (close-up)). It provides a good estimate of P_c but its computation considers only a subset of A_c , namely the edges in MST_c . As a consequence, P_{tmp_c} may not be optimal everywhere and make detours as for instance in the middle of Figure 5 (close-up) where the red line represents the shortest path.

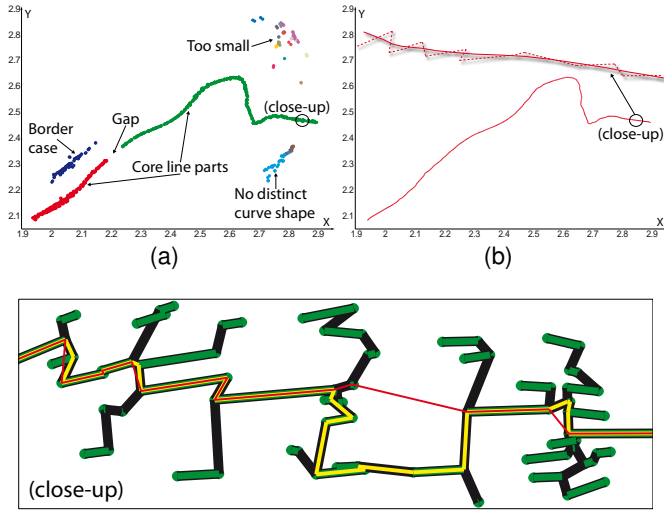


Fig. 5. Vortex core line enhancement. (a) Core line segments are clustered. (close-up) For each larger cluster, the shortest path (red) from end to end along the line segments (green) is computed based on the cluster's minimal spanning tree (black) and its longest shortest path (yellow). Note that segment overlaps result from 3D to 2D projection. (b) Gaps are closed, the path is smoothed, and small clusters representing noise and those without a distinct curve shape are neglected.

(4) Hence, the path search is extended to A_c and point pairs in the ε -neighborhood of P_{tmp_c} 's terminal vertices. Note that the two terminal vertices are located at either "end" of the cluster due to the definition of MST_c . For all point pairs, the shortest path is computed [12] and the longest of the shortest is chosen as P_c (red path in Fig. 5 (close-up)).

Verification Step. Clusters without a distinct curve shape, i.e. a high percentage of segments deviates strongly from P_c , shall be neglected from further processing since they are likely to represent false positives. At first, the median of all distances \tilde{d} between two neighboring points on P_c is computed. Then, all points in c which are not part of P_c and further off P_c than \tilde{d} are determined. For each of these points, its closest point on P_c is computed. If the share of unique closest points in total points of P_c exceeds a threshold T_2 , c is neglected since it shows a high degree of dispersion which is not restricted to a small region along P_c . A locally high dispersion is tolerable. It is occasionally observed close to the vessel wall where core line extraction is error-prone due to small velocities. The light and the dark blue clusters in Figure 5(a) fail the verification step. The latter is a border case which becomes more apparent in a 3D view.

Path Merging and Smoothing. The merging step checks whether ends of paths are close together and oriented in a similar direction. If so, the paths are likely to belong to the same core line and they are merged (paths of red and green cluster in Fig. 5(a) are merged in Fig. 5(b)). The similarity of direction is checked based on the dot product of direction vectors extracted from the paths' ends. Two thresholds T_3 and T_4 are applied to proximity and similarity of direction, respectively. In a final step, a low-order smoothing spline is fit to each path based on an automatically determined amount of smoothing [15] (Fig. 5(b)). As argued in [19], this eliminates high frequency noise, i.e., the stair-case artifacts caused by the discontinuities between neighboring segments, while maintaining the core line's curvature.

5.3 Parameter Sensitivity Analysis

A parameter sensitivity analysis was conducted to determine the stability of the enhancement result as well as default values for $T_1 - T_4$. In a visual inspection of 17 aneurysm cases with differing number of vortices, streamlines were integrated from each cluster of line segments produced by DBSCAN. If the lines were swirling around the segments, this cluster was tagged as vortex. None of the clusters was seen to represent more than one vortex indicating a good separability of the data

and performance of DBSCAN. From 94 clusters, 42 were tagged as vortex and 9 as embedded vortex. To initialize T_1 and T_2 properly, the number of points per cluster and the share of unique closest points from the verification step were opposed in a plot (Fig. 1 of the supplemental material). It reveals that vortices cannot perfectly be separated using T_1 and T_2 . However, setting $T_1 = 26$ points and $T_2 = 15\%$ achieves a good trade-off between false-positives and -negatives and only neglects two small vortices. While the inclusion of embedded vortices, which only appear on longer core lines ($T_1 > 100$ points) with a very distinct curve shape ($T_2 < 5\%$), is insensitive to slight parameter changes, the inclusion of other vortices is sensitive. In future work, an automatic vortex verification will obviate T_1 and T_2 [20].

The stability of the core line merging step has been investigated by setting T_1 and T_2 to their default values and letting T_3 vary over multitudes of ε starting by a value close to zero and terminating at half the largest diameter of the aneurysm sac. With each value of T_3 , the similarity of direction of core line ends (T_4) being closer together than T_3 was recorded. Only values in the range $[0, 1]$ (0 = orthogonal ends and 1 = collinear ends) were considered. The results are given in Figure 2 of the supplemental material. Merging only occurs for five cases and does not start until $T_3 = 1.5\varepsilon$. Multiple merges were observed for two datasets (pink and turquoise). The merges at values of $T_4 < 0.9$ were visually identified as false merges fusing unique vortices. The data at hand suggests that a combined thresholding of distance and direction at $T_3 = 1.5\varepsilon$ and $T_4 = 0.9$ (equal to $\approx 26^\circ$ maximum deviation) yields satisfying results. Small changes of T_3 and T_4 do not effect the results.

5.4 Streamline Integration

We seeded streamlines in the vicinity as well as directly on the core line and found that the latter sufficiently conveys the structure of embedded vortices. Hence, seed points are computed along each core line by equidistant resampling employing half the minimum distance between any two consecutive points in P_c . A 5th order Runge-Kutta method is employed for streamline integration. The maximum integration length is set to three times the maximum edge length of the volume mesh's bounding box. This high value accounts for the high vorticity of the investigated flow. The integration is carried out in backward and forward direction and each resulting pair of lines is merged.

6 GROUPING OF STREAMLINES

The grouping requires the computation of all equilibrium points along a core line (Sec. 6.1) and then, classifies streamlines based on the position of their respective seed point relative to the equilibrium locations (Sec. 6.2). Since equilibria subdivide a core line into regions of coherent flow transport, this structured processing ensures that all parts of embedded vortical flow are captured by a separate group of streamlines. This was confirmed by three observations in a visual investigation of 9 embedded vortices. Streamlines seeded on (see Fig. 6)

1. either side of an equilibrium point differ strongly in shape.
2. the same side exhibit a very similar shape in the vicinity of the core line and may only diverge further off.
3. two different vortex core lines differ strongly in shape unless they are traced for a long time and participate in both vortices.

Here, "shape of a streamline" refers to its progression along the vortex core line. For instance, in Figure 6(b), all green streamlines swirl in from the left of the node and at the node (between green and red arrow), jointly spiral outwards. Therefore, their shape is said to be similar. Note that for the grouping, similarity considerations are restricted to the vicinity of the core line. In the clustering-based refinement step (Sec. 7), they are extended to the entire aneurysm to capture differences further off the core line (yellow arrows in Fig. 6).

6.1 Detection of Equilibrium Points

So far, equilibria were detected visually based on color mapping the velocity magnitude onto the core line, clamping values > 1 cm/s, and searching for local minima [3]. We maximize comparability with [3]

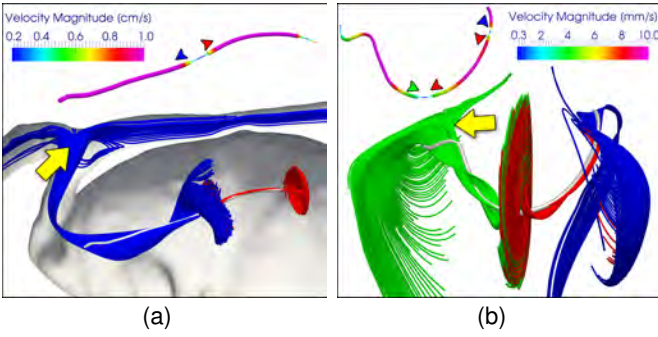


Fig. 6. Sets of streamlines seeded at two (a) and three (b) different core line parts. Lines within a set exhibit a similar shape and only diverge further off the core line (yellow arrows). The core lines are shown at their real location (gray tubes) as well as in a shifted display. In the latter, the in-/outflow direction at equilibria is depicted by arrows whose color corresponds to streamline color. Furthermore, the core line parts employed for seeding are rendered thicker.

by adopting their color mapping. The classification of equilibria, i.e., saddle or node, was achieved by integrating streamlines from manually selected core line segments only in forward or backward direction.

The strict calculation and classification of equilibria/critical points in vector fields with a finite precision suffers from numerical instabilities. We suggest a more robust alternative that is based on analyzing the local flow transport (insets/outsets) along the core line. Before we describe the approach, we characterize the types of equilibria that were observed in our case studies.

Types of Equilibrium Points. The following types are indicated by colored spherical glyphs in all visualizations (e.g., Fig. 9):

- $\leftarrow \circ \rightarrow$, saddle point (\circ), two unstable outsets ($\leftarrow \rightarrow$)
- $\rightarrow \circ \leftarrow$, stable node, two stable insets
- $| \circ \rightarrow$, end of core line near wall ($|$), one unstable outset
- $\circ \rightarrow$, end of core line offside wall, one unstable outset

In accordance with [14], we observed equilibria at the ends of vortex cores, particularly, at those anchored to the aneurysm wall. Here, wall-near flow is advected in a swirling motion, leaves the wall along the outset, and spirals along the core line. Detecting these equilibria is desirable since the inner vortex of an embedded vortex may originate here and not as typical, at a saddle (e.g., left blue sphere in Fig. 9(a,g)).

Detection based on Normalized Helicity. While detecting equilibria as local minima in a function of clamped velocity magnitude $|\vec{v}|$ over core line points (plot in Fig. 7) may seem straightforward, it fails in two situations (topmost core line in Fig. 7). First, equilibria within larger “stagnation zones”, such as the left large dark blue zone, may not be reflected by distinct minima (plot). However, the velocity vectors \vec{v} in this zone point in alternating directions of flow transport indicating the presence of equilibria (encircled close-up). Second, multiple equilibria, i.e. local minima, may exist within a region of very low velocity magnitude, such as those within the stagnation zone plus the one within the smaller dark blue zone to its right.

Our solution is inspired by the visual separation of a primary and an embedded secondary vortex based on the switching sign of *normalized helicity* in [11]. Helicity is defined as the knottedness of *vortex lines* [27]. These lines are everywhere tangent to the vorticity vector $\vec{\omega} = \nabla \times \vec{v}$ which describes the curl of the flow velocity. Normalized helicity H is computed as:

$$H = \vec{\omega} \cdot \vec{v} / (|\vec{\omega}| |\vec{v}|), \in [-1, +1] \quad (1)$$

The sign of H is negative if \vec{v} and $\vec{\omega}$ point in an opposite direction and positive if they point in the same direction. This property is exploited in detecting the equilibria. Since the direction of $\vec{\omega}$ is stable

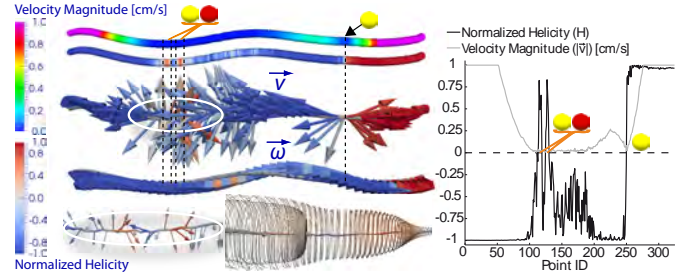


Fig. 7. Detection of nodes and saddles (red and yellow spheres) based on normalized helicity H and velocity magnitude $|\vec{v}|$ along the vortex core line. H is the normalized dot product of \vec{v} and vorticity vector $\vec{\omega}$. All vectors are scaled to unit length to improve readability. Equilibria are more reliably indicated by zero crossings of H than by minima of $|\vec{v}|$.

along the core line and the direction of \vec{v} switches at both, saddles and nodes (Fig. 7), equilibria are indicated by zero crossings in a function of H over core line points (plot in Fig. 7). The precise positions of the equilibria are gained by interpolation based on the respective two points “enclosing” a crossing and their values of H . Finally, the equilibria are classified by comparing the average direction of \vec{v} on either side in a local neighborhood. For a saddle, the dot product of the two average vectors is negative while it is positive for a node.

The detection of equilibria based on H and $|\vec{v}|$ is compared in Figure 7. Two saddle-node pairs within the stagnation zone and the nearby saddle are identified using H . The pairs would have been missed employing $|\vec{v}|$. They form two adjacent embedded vortices with one enveloping the other (illustrated by streamlines). The analysis of H is also more robust since zero crossings are global features of a function and hence, less sensitive to low frequency jags than local minima.

Detection at Vortex Core Line Ends. Equilibria at core line ends are not reflected by a switching sign of H due to the unidirectional flow there. However, they are located inside small regions with $|\vec{v}| < 1$ cm/s (clamping value). If such a region exists, its point with minimum $|\vec{v}|$, which in all cases corresponded to the terminal vertex of the core line, is taken as equilibrium point. Depending on its distance to the aneurysm wall, it is classified as “near wall” or “offside” wall (blue or green sphere).

6.2 Grouping

This step iterates over all vortex core lines, partitions them according to the respective equilibria, and assigns each streamline to a partition.

Grouping at Saddles and Nodes. Only saddles and nodes are considered for the partitioning since only streamlines seeded on either side of these equilibria differ strongly in shape (Fig. 6). Accordingly, the core line in Figure 7, is divided by the five equilibria into six partitions. Before streamlines are assigned to them, *safety margins* are defined around saddles and nodes (thin parts of exposed core lines in Fig. 6). They account for the potential inaccuracies involved in core line extraction and enhancement and comprise all core line points within the next five penetrated volume elements to either side.

Streamlines seeded outside the safety margins are assigned to the partition containing their respective seed point thereby creating initial streamline groups. For each group, a *representative* is determined employing our variant [32] of *density-based representatives* [31]. In short, the longest streamline traversing the densest parts of the group is computed. For streamlines seeded inside the margins, the similarity to the neighboring group representatives is calculated based on minimum closest point distances. Each line is then assigned to the group of the most similar representative and finally, all representatives are updated.

Grouping at Near-Wall Equilibria. Group representatives shall convey each distinct streamline shape occurring in the vicinity of the core line. To guarantee this at near-wall equilibria, a refinement step is necessary. At the corresponding core line end, two types of streamlines are observed (arrow in upper inset of Fig. 9(g)): longer lines whose backward integration indicates the inflow of the vortex and

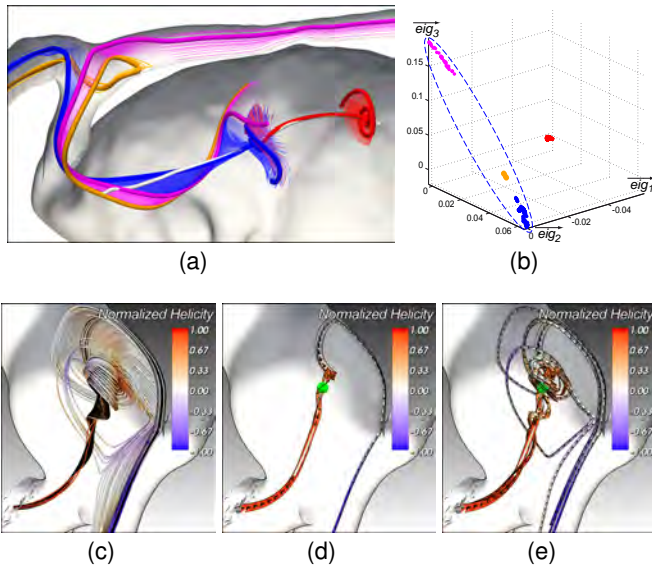


Fig. 8. Clustering-based refinement. (a) The streamline groups in Figure 6(a) were refined based on their spectral embedding (b). The encircled clusters constitute the blue group in Figure 6(a). (c) Streamlines at a vortex without an embedded structure were grouped in (d) and the groups were refined in (e) yielding a comprehensive representation.

short lines whose backward integration terminated early due to near-zero velocities close to the aneurysm wall. To ensure that representatives convey both types, the streamline group that has been assigned to the partition containing the core line end is split according to the length of the backward integrated streamline part. The set of lengths forms two crisp clusters that can be detected by k-means with $k = 2$. The two corresponding subgroups of streamlines replace the current group and their representatives are computed. In the lower inset of Figure 9(g), the upper and the lower arrow point at the representative indicating the inflow and the early terminated streamlines, respectively.

Grouping at Core Lines with a Single Equilibrium Point.

We observed core lines with a single equilibrium located at one of their ends, mostly near the wall and once, offside the wall (Fig. 9(b) and 9(e)). We chose to generate two representatives per such core line so that their intertwining conveys the vortical nature of the flow. For core lines with a near-wall equilibrium, k-means clustering as described above is employed. For the rest, the density-based representative of all associated streamlines is first computed. Next, the similarity of all lines to the representative is calculated and the similarities are clustered using k-means with $k = 2$. Finally, the representatives of both clusters are computed, one conveying the densest part of the streamline group and one conveying the part that deviates most from it.

7 CLUSTERING-BASED GROUP REFINEMENT

The clustering-based refinement of streamline groups allows for a more detailed visualization of flow further off the core line and of vortical flow without an embedded structure. In previous work, we showed that *spectral clustering* of streamlines generates expressive blood flow summaries [32]. Here, we recapitulate the approach and explain its adaptation to the refinement of an initial grouping result.

7.1 Spectral Clustering

Spectral clustering (SC) maps all streamlines to a *spectral embedding space* where each line is represented by a point (Fig. 8 (a,b)). This mapping preserves local distance relations and increases cluster separability. SC starts by constructing a $n \times n$ symmetric *distance matrix* \mathbf{M} that contains all pair-wise distances/dissimilarities between n streamlines. Then, the $n \times n$ *affinity matrix* \mathbf{W} is constructed by applying a function f to the entries of \mathbf{M} . As f , a Gaussian is used assigning high affinities to low distances and vice versa. Based on \mathbf{W} , the

$n \times n$ *Graph Laplacian* \mathbf{L} is computed [51]. Then, the k largest eigenvalues and their corresponding eigenvectors of \mathbf{L} are determined with k representing the number of clusters. These eigenvectors span the k -dimensional spectral embedding space (Fig. 8(b)). Instead of providing k , a range of values $[a, b]$ is provided by the user. The optimum number of clusters within $[a, b]$ and a cluster label per streamline are then returned by an *eigenvector rotation* approach [51].

7.2 Group Refinement

Our adaptation of SC employs the grouping result to constrain the clustering-based refinement. Since streamlines from different groups exhibit a considerably different shape, they must not fall into the same cluster. As a consequence, distances in \mathbf{M} must only be computed for pairs of streamlines from the same group. To speed up distance computation, *hierarchical signatures* [26] are employed. Distances between lines from different groups are set to a predefined very high value such that the Gaussian f is evaluated to zero (affinity). The remaining steps are identical to our previous approach except for the initialization of $[a, b]$. Instead of assigning an arbitrary minimum to a , it is set to the number of streamline groups. Assuming that each group will not be partitioned more than the number of draining vessels dv , b is set to $a * dv$. Constraining SC yields a performance gain due to fewer distance computations. In the best case, the g streamline groups are of equal size reducing the number of computations by factor $\approx g$.

The streamline groups in Figure 6(a) were refined in Figure 8(a), yielding a separate cluster for each unique streamline shape. Representatives now well convey the fact that flow leaving the vortex proceeds through different draining vessels. The spectral embedding of the streamlines reflects the four well-separable clusters (Fig. 8(b)). In Figure 8(c), streamlines convey vortical flow without embedded structure. The corresponding core line exhibits a single equilibrium at one of its ends offside the aneurysm wall (green sphere) and the streamlines were grouped accordingly (Fig. 8(d)). While the two group representatives partially convey the vortex, the group refinement yields a more comprehensive representation (Fig. 8(e)).

8 VISUAL SUMMARY OF VORTICAL FLOW

We describe the aggregation of group/cluster representatives in a visual summary of vortical flow, present exploration techniques, and demonstrate the summary in six case studies. We use the term cluster to refer to both, group and cluster. Exemplary summaries are shown in Figure 9(g-j). In Section 2 of the supplemental material, we report on timings of generating the summary.

8.1 Composition of the Visual Summary

Stream ribbons and tubes have been tested for visualizing the cluster representatives. While tubes allow for a good readability of color-mapped parameters independent of the viewpoint, we favor ribbons since they additionally encode the local curl of the flow. A narrow strip of polygons is added to each representative streamline. Its curl is either determined by the local vorticity vectors or by normal vectors, which are forced to minimally rotate along the line. The former yields strongly twisted ribbons in regions of high vorticity hampering the readability of color and textures. The latter resolves this problem but indicates the torsion of the streamline instead of the flow's local curl. Hence, both opportunities were integrated. The latter is shown in the paper to avoid readability issues.

The width of a ribbon encodes the number of streamlines in its associated cluster. Black halos improve the visual separability of the ribbons. An arrowhead glyph is attached to the ribbon's end that points in outflow direction. To visualize the local flow direction at equilibria, arrow textures are mapped onto the ribbons inspired by [44]. Normalized helicity H (Eq. 1) is mapped along the ribbons by a diverging blue-to-red color scale. The display of representatives is embedded in a surface rendering of the aneurysm. The front faces are culled to provide an unobstructed view. A silhouette drawing lets the surface stand out from the background. The streamlines of a cluster can be displayed to indicate its extent. They are rendered with GPU support, black halos are added to improve spatial perception [13], and normalized helicity

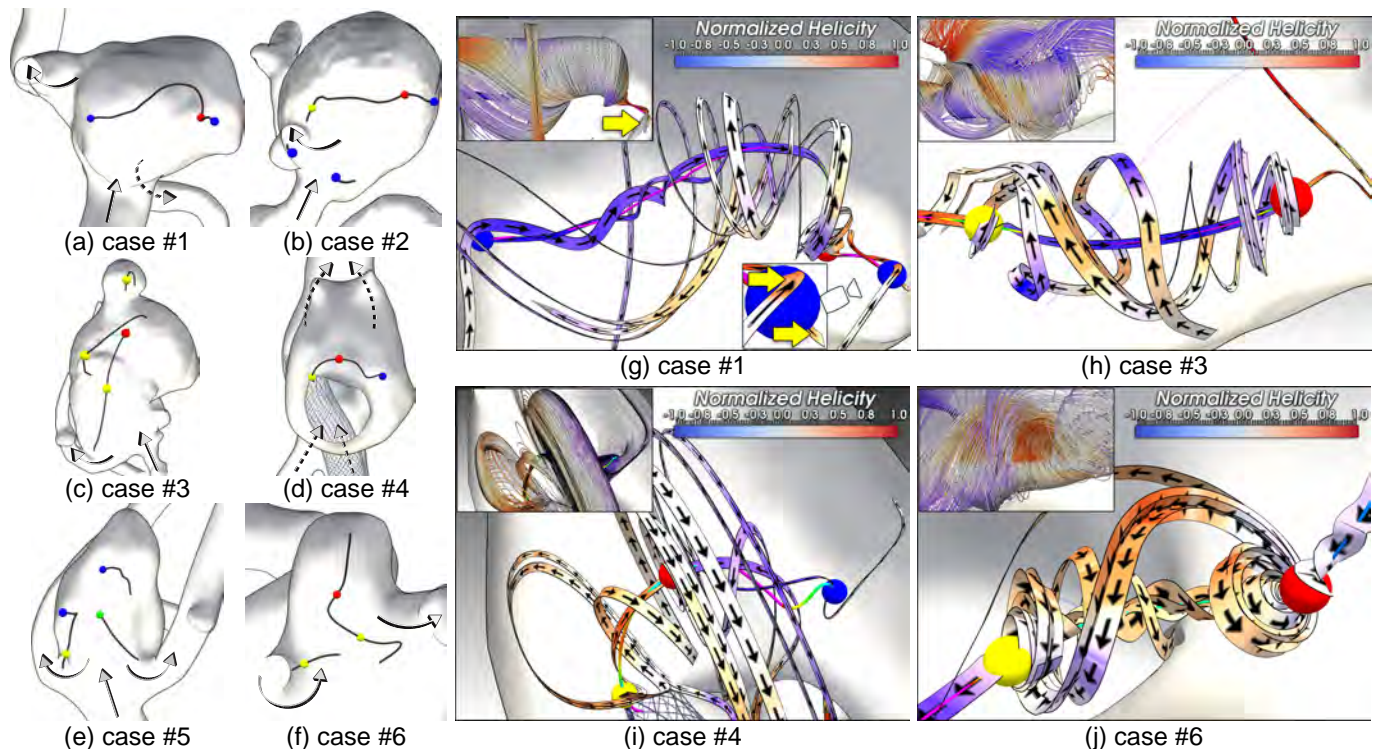


Fig. 9. The cases analyzed in this work are presented in the first two columns. Aneurysmal morphology including feeding and draining arteries, inflow and outflow direction (arrows), vortex core lines (dark gray tubes), equilibrium points (colored spheres), and a stent (wire mesh in (d)) are depicted. Embedded vortices are shown in detail views of selected visual summaries of vortical flow in the last two columns. Insets depict the original streamlines. The lower inset of (g) shows a near-wall equilibrium (blue sphere) and the representatives of the two types of streamlines (arrows) which are typically observed here (Sec. 6.2). In the corresponding upper inset, an arrow points at the represented streamlines.

is color-coded (insets of Figure 9(g-j)). Inspired by [14], equilibria are represented by spherical glyphs whose color encodes the type of equilibrium (Sec. 6.1). Vortex core lines are rendered as tubes and colored according to velocity magnitude as described in Section 6.1.

8.2 Exploration of the Visual Summary

The exploration techniques discussed in [32] and two new techniques are integrated. First, an inspection of the flow in the immediate vicinity of an equilibrium point is supported. Clicking on the spherical glyph causes an emphasis of the two representatives associated with the adjacent core line partitions. Second, investigating flow in the presence of multiple vortices benefits from a smart visibility strategy. Please, see the supplemental video for a demonstration. In an overview visualization, the representatives of all vortices are displayed. As the user zooms in on a vortex, all other vortices gradually disappear. This is realized by coupling opacity with distance to the camera. A proper functioning requires that the vortex of interest is always closest to the camera and in the approximate center of the viewport. Once the distance is < 4 mm, the representatives of the vortex in focus also start to fade-out and its spherical glyphs gradually shrink to reveal the core line and facilitate an inspection of its velocity magnitude profile.

8.3 Case Studies

We processed 17 cerebral aneurysm cases from which we chose six representative ones for illustration (Fig. 9(a-f)). Visual summaries of selected additional cases are shown in the supplemental material (Sec. 4). The six cases differ with respect to location at the circle of Willis, type: side-wall (cases #4, case #6) vs. basilar tip (the rest), size: small (case #6) vs. giant (case #3) vs. big (the rest), and number of vortices. Furthermore, case #4 was virtually stented and case #2 exhibits a local outpouching (*bleb*) at the top of the aneurysm sac.

For each of the first three cases, at least one embedded vortex had been observed in unsteady CFD simulation data. To study the structure of the vortex at full manifestation, a representative point of the cardiac

cycle was selected. For the last three cases, only steady-state CFD simulation data existed. A candidate embedded vortex was observed in case #6. For case #4, no clear statement could be made since the outer layers of two adjacent candidate embedded vortices only briefly envelope their inner counterpart before leaving the aneurysm. No embedded vortex seems to exist in case #5. A conclusive assessment of the three cases yet requires unsteady data covering the cardiac cycle.

Detail views of the visual summaries of vortical flow are presented for case #2 in Figure 1(g), for case #5 in Figure 8(c-e), and for the remaining cases in Figure 9(g-j). Each summary has been visually validated by our collaborators. The correctness of the groups/clusters and their representatives was assessed based on a display of the corresponding original streamlines and on additional arrow glyphs conveying the flow direction along the core line as well as along the streamlines. The glyphs helped in validating the determined type of equilibrium as well as the orientation of the ribbon textures. All visual summaries were assessed as correct. Note that this assessment neglects vortices potentially missed during core line extraction (Sec. 5.1). The false-positive and -negative core line candidate clusters described in Section 5.3 do not affect the six demonstration cases.

We restrict our discussion to cases exhibiting a definite embedded vortex (candidate). While case #2, case #3, and case #6 show the typical saddle-node configuration (yellow and red sphere), the inner vortex of case #1 originates at a near-wall equilibrium (left blue sphere). The latter configuration must be considered in embedded vortex detection since core lines of strong vortices are frequently attached to the aneurysm wall and end their in an equilibrium [14]. A single embedded vortex had been reported for the ruptured *giant aneurysm* case #3 [3]. We found two more embedded vortices (Sec. 6.1, Fig. 7). However, both together reach their full extent at a different point of the cardiac cycle and are small-scale phenomena compared to the known vortex (Fig. 9(h)). Hence, they are neglected here and their equilibria are not shown in Figure 9(c). Case #6 in Figure 9(f) had been investigated in previous work [32]. While the swirl in the center of

Table 1. The visual summary *VS* of vortical flow was compared to interactively seeding *IS* streamlines at selected core line parts and spectral clustering *SC* of streamlines and display of cluster representatives [32].

Analysis Time [m:s]			Correct Equilibrium Classification [%]			Embedded Vortex Detection [%]		
IS	SC	VS	IS	SC	VS	IS	SC	VS
9:24	5:36	2:06	90	76	100	95	100	100
Convenience of Analysis [-2,+2]			Confidence in Analysis Results [-1,+1]			Clarity of Visualization [-2,+2]		
-0.4	-0.1	1.3	0.0	0.1	0.8	-0.6	0.5	1.3

the aneurysm was observed, details of the swirling motion remained hidden. Accordingly, the embedded vortex along the upper core line (Fig. 9(j)) had been described just as “complex flow”.

9 EVALUATION

We carried out an evaluation comparing our new and two prior approaches with regard to the quality and speed of detecting embedded vortices and equilibria as well as of characterizing the flow near equilibria. We compared (*VS*) our visual summary without the clustering-based group refinement, (*IS*) the interactive seeding of streamlines at selected core line parts as in [3] (Sec. 4), and (*SC*) the spectral clustering of streamlines and display of cluster representatives [32]. *IS* is employed by our collaborators and has been reimplemented in ParaView (Kitware, Clifton Park, NY). For *SC*, we used our in-house implementation. Since the core line enhancement is not part of *IS* and *SC*, the originally extracted core line segments were employed as seeding geometry for both (Sec. 5.1). They were rendered and colored according to velocity magnitude in order to indicate equilibria [3]. Seeding regions as well as integration direction and length could be modified in *IS*. In *SC*, individual representatives could be turned on/off and streamlines could be displayed for each cluster. Please consult Section 3 of the supplemental material for illustrating screenshots.

Two CFD engineers (no co-authors) with long-term experience in analyzing blood flow and eight computer scientists with a background in flow visualization participated in the evaluation. Each session started with a briefing including the definition of embedded vortices and equilibria and a short introduction. Then, each participant employed each approach twice to analyze all six cases (Fig. 9(a-f)). A questionnaire had to be filled in per case showing the vortex core lines inside a drawing of the aneurysm. Participants were asked to encircle core lines exhibiting embedded flow, sketch inner and outer vortex, indicate the equilibria and determine their type (Sec. 6.1). Since spherical glyphs represent equilibria in *VS*, the participants were asked here to validate their location and classification. Finally, they rated the convenience of the analysis process, their confidence in the results, and the visual clarity of the visualization. The analysis process was timed.

The evaluation results are summarized in Table 1. On average, *VS* reduces the analysis time by a factor of ≈ 4.5 and ≈ 2.7 as compared to *IS* and *SC*, respectively. Participants spent plenty of time in *SC* with deducing local flow direction at an equilibrium from the arrowheads’ direction of the corresponding representatives (Fig. 3(b)). In *VS*, this information is locally encoded by arrow textures (Fig. 1(g)). The participants detected all equilibria in all cases independent of the applied approach. Hence, the detection rates are omitted and only the classification rates are given. In *VS*, all equilibria were confirmed as properly localized and classified. The classification rate in *IS* was also high while only 76% of the equilibria were classified correctly in *SC*. This is due to an inadequate visualization of flow (direction) at some equilibria (Fig. 3). Participants were explicitly asked not to guess the flow (direction) but only to report what they actually see. All embedded vortices were detected in *VS* and *SC*. One participant did not observe the embedding in case #3 (Fig. 9(h)) based on *IS*. Some participants saw an embedded vortex in the ambiguous case #4, while others did not (Fig. 9(i)). Both answers were counted as correct. The convenience of the analysis was rated highest for *VS* with a substantial lead on *SC* and *IS*. The participants had great trust in their analysis results based on *VS* but felt less confident when employing *IS* and *SC*. Furthermore, the visual clarity of *VS* was rated highest. In *IS*, participants

complained about the cluttered streamline display while in *SC*, they found parts of vortical flow not properly conveyed (Fig. 3).

Limitations. The evaluation has the character of first preliminary tests. A prospective user study will be based on a larger database of aneurysms ($n = 210$) capturing the variety of location, shape, and hemodynamics [7]. It will involve more and a wider variety of users, e.g., neurosurgeons and neuroradiologists. Since expert users will employ our approach, participants should be familiar with flow visualization and analysis. So far, the evaluation focused on the streamline grouping step whose results are sufficient for conveying the global structure of embedded flow and the location and type of equilibria. The prospective study will include the group refinement step.

A reworked study design will ensure that metrics such as analysis time are not biased towards *VS*, which is designed to highlight vortices and equilibria. Instead, users will be asked to accomplish the tasks employing *IS* and *SC* and their results will be compared to those of our new pipeline (Fig. 4). Our case studies indicate that the pipeline can batch the database and solve the tasks automatically. The generated quantitative results will be compared to the manually derived ones and the visual summaries *VS* will be rated by the users.

Given a positive evaluation of *VS*, an insight-based study will be conducted with expert users. For this purpose, *VS* will be integrated in an analysis system [30] and embedded in a more realistic data analysis context. More general analysis tasks will aim at understanding the effects of (embedded) vortical flow on quantitative hemodynamic parameters, such as pressure and *wall shear stress*, and the relation to other qualitative parameters, such as wall-near flow and the *inflow jet* [17]. In pair analytics sessions, an expert user and a developer will analyze the data and try to generate application-specific insight and hypotheses. Both will be counted yielding metrics of success.

10 SUMMARY AND OUTLOOK

We presented a pipeline for the cluster-based visual analysis of vortical flow in simulated cerebral aneurysm hemodynamics. Segments of vortex core lines affected by artifacts are transformed into continuous core lines serving as a basis for seeding streamlines that convey the vortical flow. Streamlines are grouped and group representatives are computed such that each distinct flow behavior in the vicinity of the core line is properly captured. On demand, the groups are refined yielding a more detailed representation of more distant flow. The group/cluster representatives are aggregated in a visual summary of vortical flow.

With the focus on embedded vortices, the pipeline was applied to 17 aneurysm cases from which six were chosen for demonstration here. The corresponding visual summaries were positively evaluated by experts. They outperform the summaries generated by our previous approach [32] in terms of production time and accuracy. Our collaborating CFD engineers so far managed to manually investigate a few cases a day. Assuming an automated, reliable vortex core line extraction, the pipeline facilitates a batch processing of their database ($n = 210$) [7].

Relating embedded vortices to aneurysm rupture and hemodynamic parameters may contribute to an understanding of their implications, which may range from thrombosis initiation to high/low wall shear stress. However, this requires extending the considered time-window from one point in time to the full cardiac cycle. This will pose further challenges such as tracking saddle-node bifurcations over time [41].

Our results strongly depend on the vortex core line extraction and enhancement. While for the extraction no perfect criterion or algorithm delivering a ground truth exist [1], we carried out a parameter sensitivity analysis for the enhancement step. The resulting default values of all involved parameters yielded satisfactory results for the 17 cases. The parameters of streamline grouping and clustering-based group refinement influence the summaries rather slightly. No adjustment of their proposed default values was required.

ACKNOWLEDGMENTS

The authors wish to thank G. Byrne, T. Günther, and H. Theisel for the fruitful discussions on flow topology. This work was partly funded by the Federal Ministry of Education and Research in Germany within the Research Campus STIMULATE under grant number 03FO16102A.

REFERENCES

- [1] A. Biswas, D. Thompson, W. He, Q. Deng, C.-M. Chen, H.-W. Shen, R. Machiraju, and A. Rangarajan. An uncertainty-driven approach to vortex analysis using oracle consensus and spatial proximity. In *PacificVis*, accepted, 2015.
- [2] S. Born, M. Markl, M. Gutberlet, and G. Scheuermann. Illustrative visualization of cardiac and aortic blood flow from 4D MRI data. In *PacificVis*, pages 129–136, 2013.
- [3] G. Byrne and J. R. Cebral. Vortex dynamics in cerebral aneurysms. *arXiv:1309.7875v1*, 2013.
- [4] G. Byrne, F. Mut, and J. R. Cebral. Quantifying the large-scale hemodynamics of intracranial aneurysms. *AJNR Am J Neuroradiol*, 35(2):333–338, 2014.
- [5] J. R. Cebral, M. A. Castro, S. Appanaboyina, C. M. Putman, D. Milan, and A. F. Frangi. Efficient pipeline for image-based patient-specific analysis of cerebral aneurysm hemodynamics: Technique and sensitivity. *IEEE Trans Med Imaging*, 24(4):457–467, 2005.
- [6] J. R. Cebral, F. Mut, J. Weir, and C. Putman. Quantitative characterization of the hemodynamic environment in ruptured and unruptured brain aneurysms. *AJNR Am J Neuroradiol*, 32(1):145–151, 2011.
- [7] J. R. Cebral, F. Mut, J. Weir, and C. M. Putman. Association of hemodynamic characteristics and cerebral aneurysm rupture. *AJNR Am J Neuroradiol*, 32(2):264–270, 2011.
- [8] C.-K. Chen, S. Yan, H. Yu, N. Max, and K.-L. Ma. An illustrative visualization framework for 3D vector fields. *Comput Graph Forum*, 30(7):1941–1951, 2011.
- [9] J. Crawford. Introduction to bifurcation theory. *Rev. Mod. Phys.*, 63:991–1037, 1991.
- [10] M. Daszykowski, B. Walczak, and D. Massart. Looking for natural patterns in data: Part 1. Density-based approach. *Chemometr Intell Lab Syst*, 56(2):83–92, 2001.
- [11] D. Degani, A. Seginer, and Y. Levy. Graphical visualization of vortical flows by means of helicity. *AIAA journal*, 28(8):1347–1352, 1990.
- [12] E. W. Dijkstra. A note on two problems in connexion with graphs. *Numerische Mathematik*, 1(1):269–271, 1959.
- [13] M. H. Everts, H. Bekker, J. B. Roerdink, and T. Isenberg. Depth-dependent halos: Illustrative rendering of dense line data. *IEEE Trans Vis Comput Graphics*, 15(6):1299–1306, 2009.
- [14] A. Gambaruto and A. João. Flow structures in cerebral aneurysms. *Computers & Fluids*, 65:56–65, 2012.
- [15] D. Garcia. Robust smoothing of gridded data in one and higher dimensions with missing values. *Comput Stat Data An*, 54(4):1167–1178, 2010.
- [16] C. Garth, X. Tricoche, T. Salzbrunn, T. Bobach, and G. Scheuermann. Surface techniques for vortex visualization. In *Joint Eurographics-IEEE TCVC Conference on Visualization*, pages 155–164, 2004.
- [17] R. Gasteiger, D. J. Lehmann, R. van Pelt, G. Janiga, O. Beuing, A. Vilanova, H. Theisel, and B. Preim. Automatic detection and visualization of qualitative hemodynamic characteristics in cerebral aneurysms. *IEEE Trans Vis Comput Graphics*, 18(12):2178–2187, 2012.
- [18] S. Glaßer, K. Lawonn, T. Hoffmann, M. Skalej, and B. Preim. Combined visualization of wall thickness and wall shear stress for the evaluation of aneurysms. *IEEE Trans Vis Comput Graphics*, pages 2506–2515, 2014.
- [19] M. Jankun-Kelly, M. Jiang, D. Thompson, and R. Machiraju. Vortex visualization for practical engineering applications. *IEEE Trans Vis Comput Graphics*, 12(5):957–964, 2006.
- [20] M. Jiang, R. Machiraju, and D. Thompson. Geometric verification of swirling features in flow fields. In *IEEE Visualization*, pages 307–314, 2002.
- [21] M. Jiang, R. Machiraju, and D. Thompson. *The Visualization Handbook*, chapter Detection and Visualization of Vortices, pages 295–309. Elsevier, Amsterdam, 2005.
- [22] D. B. Johnson. Efficient algorithms for shortest paths in sparse networks. *Journal of the ACM*, 24(1):1–13, 1977.
- [23] B. Köhler, R. Gasteiger, U. Preim, H. Theisel, M. Gutberlet, and B. Preim. Semi-automatic vortex extraction in 4D PC-MRI cardiac blood flow data using line predicates. *IEEE Trans Vis Comput Graphics*, 19(12):2773–2782, 2013.
- [24] R. S. Laramée, D. Weiskopf, J. Schneider, and H. Hauser. Investigating swirl and tumble flow with a comparison of visualization techniques. In *IEEE Visualization*, pages 51–58, 2004.
- [25] R. Löhner. Automatic unstructured grid generators. *Finite Elem Anal Des*, 25(12):111–134, 1997. Adaptive Meshing, Part 1.
- [26] T. McLoughlin, M. W. Jones, R. S. Laramée, R. Malki, I. Masters, and C. D. Hansen. Similarity measures for enhancing interactive streamline seeding. *IEEE Trans Vis Comput Graphics*, 19(8):1342–53, 2013.
- [27] H. K. Moffatt. The degree of knottedness of tangled vortex lines. *J Fluid Mech*, 35(1):117–129, 1969.
- [28] F. Mut, R. Aubry, R. Löhner, and J. R. Cebral. Fast numerical solutions of patient-specific blood flows in 3D arterial systems. *Int J Numer Method Biomed Eng*, 26(1):73–85, 2010.
- [29] F. Mut, R. Löhner, A. Chien, S. Tateshima, F. Viuela, C. Putman, and J. R. Cebral. Computational hemodynamics framework for the analysis of cerebral aneurysms. *Int J Numer Meth Bio*, 27(6):822–839, 2011.
- [30] M. Neugebauer, K. Lawonn, O. Beuing, P. Berg, G. Janiga, and B. Preim. Amnvis—a system for qualitative exploration of near-wall hemodynamics in cerebral aneurysms. *Comp Graph Forum*, 32(3pt3):251–260, 2013.
- [31] L. O’Donnell, A. J. Golby, and C.-F. Westin. Tract-based morphometry for white matter group analysis. *NeuroImage*, 45:832–844, 2009.
- [32] S. Oeltze, D. J. Lehmann, A. Kuhn, G. Janiga, H. Theisel, and B. Preim. Blood flow clustering and applications in virtual stenting of intracranial aneurysms. *IEEE Trans Vis Comput Graphics*, 20(5):686–701, 2014.
- [33] F. H. Post, B. Vrolijk, H. Hauser, R. S. Laramée, and H. Doleisch. The state of the art in flow visualisation: Feature extraction and tracking. *Comput Graph Forum*, 22(4):775–792, 2003.
- [34] R. C. Prim. Shortest connection networks and some generalizations. *AT&T Tech J*, 36(6):1389–1401, 1957.
- [35] F. Sadlo, R. Peikert, and M. Sick. Visualization tools for vorticity transport analysis in incompressible flow. *IEEE Trans Vis Comput Graphics*, 12(5):949–956, 2006.
- [36] J. Sahner, T. Weinkauff, and H.-C. Hege. Galilean invariant extraction and iconic representation of vortex core lines. In *EuroVis/IEEE VGTC Symposium on Visualization*, pages 151–160, 2005.
- [37] J. Sahner, T. Weinkauff, N. Teuber, and H.-C. Hege. Vortex and strain skeletons in Eulerian and Lagrangian frames. *IEEE Trans Vis Comput Graphics*, 13(5):980–990, 2007.
- [38] T. Salzbrunn, H. Jänicke, T. Wischgoll, and G. Scheuermann. The state of the art in flow visualization: Partition-based techniques. In *Simulation and Visualization (SimVis)*, pages 75–92, 2008.
- [39] T. Salzbrunn and G. Scheuermann. Streamline predicates. *IEEE Trans Vis Comput Graphics*, 12(6):1601–1612, 2006.
- [40] T. Schafhitzel, J. E. Vollrath, J. P. Gois, D. Weiskopf, A. Castelo, and T. Ertl. Topology-preserving λ_2 -based vortex core line detection for flow visualization. *Comput Graph Forum*, 27(3):1023–1030, 2008.
- [41] G. Scheuermann, W. Kollmann, X. Tricoche, and T. Wischgoll. *Numerical Simulations of Incompressible Flows*, chapter Evolution of topology in axi-symmetric and 3-d viscous flows, pages 622–643. World Scientific Publishing, 2003.
- [42] S. Shafii, H. Obermaier, V. Kolár, M. Hlawitschka, C. Garth, B. Hamann, and K. I. Joy. Illustrative rendering of vortex cores. In *Eurographics Conference on Visualization (EuroVis)*, pages 61–65, 2013.
- [43] S. Stegmaier, U. Rist, and T. Ertl. Opening the can of worms: An exploration tool for vortical flows. In *IEEE Visualization*, pages 463–470, 2005.
- [44] C. Stoll, S. Gumhold, and H.-P. Seidel. Visualization with stylized line primitives. In *IEEE Visualization*, pages 695–702, 2005.
- [45] D. Sujudi and R. Haimes. Identification of swirling flow in 3d vector fields. Technical Report AIAA 95-1715, Department of Aeronautics and Astronautics, MIT, Cambridge, MA, 1995.
- [46] G. Taubin. A signal processing approach to fair surface design. In *ACM SIGGRAPH*, pages 351–358, 1995.
- [47] R. F. P. van Pelt, S. S. A. M. Jacobs, B. M. ter Haar Romeny, and A. Vilanova. Visualization of 4D blood-flow fields by spatiotemporal hierarchical clustering. *Comp Graph Forum*, 31(3pt2):1065–1074, 2012.
- [48] M. H. Vlak, A. Algra, R. Brandenburg, and G. J. Rinkel. Prevalence of unruptured intracranial aneurysms, with emphasis on sex, age, comorbidity, country, and time period: A systematic review and meta-analysis. *Lancet Neurol*, 10(7):626–636, 2011.
- [49] P. J. Yim, G. B. C. Vasbinder, V. B. Ho, and P. L. Choyke. Isosurfaces as deformable models for magnetic resonance angiography. *IEEE Trans Med Imaging*, 22(7):875–881, 2003.
- [50] H. Yu, C. Wang, C.-K. Shene, and J. H. Chen. Hierarchical streamline bundles. *IEEE Trans Vis Comput Graphics*, 18(8):1353–1367, 2012.
- [51] L. Zelnik-Manor and P. Perona. Self-tuning spectral clustering. In *Advances in Neural Information Processing Systems*, pages 1601–08, 2004.